ADVANCED HEALTHCARE MATERIALS
www.advhealthmat.de

Motor-Free Soft Robots for Cancer Detection, Surgery, and In Situ Bioprinting

*Chi Cong Nguyen, James Davies, Aditya Ashok, Trung Thien Hoang, Anahid Ehteda, Tran Bach Dang, Emanuele Nicotra, Hien A. Tran, Bibhu Sharma, Kefan Zhu, Phuoc Thien Phan, Adrienne Ji, Jingjing Wan, Jelena Rnjak-Kovacina, Orazio Vittorio, Hoang-Phuong Phan, Nigel Hamilton Lovell, and Thanh Nho Do**

Recent advancements in teleoperated surgical robotic systems (TSRSs) for minimally invasive surgery (MIS) have significantly improved diagnostic and surgical outcomes. However, as the complexity of MIS procedures continues to grow, there is an increasing need to enhance surgical tools by integrating advanced functionalities into these instruments for superior medical results. Despite recent advancements, TSRSs face significant challenges, including rigidity, suboptimal actuation methods, large sizes, and complex control mechanisms. This paper presents a portable, motor-free soft robotic system equipped with soft robotic arms (SRAs) that provides an innovative solution for performing MIS within complex human organs. Unlike conventional approaches, these SRAs leverage a soft fibrous syringe architecture for operation, eliminating the need for complex control systems. This design achieves precise motion control with mean errors <300 µm, effectively minimizing physical tremors. Two SRAs—one with and one without a central lumen—are developed. By integrating microelectrodes into the SRAs, the system demonstrates capabilities to support cancer detection via electrical impedance measurements and to perform radio-frequency ablation for surgical treatments. Additionally, the system supports biomaterial injections and in situ 3D printing for internal wound healing. This simple, cost-effective platform represents a promising new direction for developing TSRSs in MIS.

1. Introduction

Lung, gastrointestinal (GI), and brain (nervous system) cancers, along with other cancers in tubular organs represent the top leading causes of cancer deaths worldwide. Presently, significant challenges emerge in early detection/diagnosis and treatment regimes.[1] Traditional diagnostic methods, including biopsy, imaging (e.g., X-ray, CT scan, and MRI), or cytology often fail to detect small tumors accurately.[2] For instance, imaging methods can yield false-positive outcomes, complicating the diagnosis and subsequent treatment plans. In situ (direct) detection using onboard electronics such as electrical impedance measurements via minimally invasive delivery techniques has emerged as a transformative solution. This approach leverages the electrical impedance spectroscopy (EIS) measured from the integrated metal electrodes at the tip of miniaturized surgical instruments to detect the tumor tissue in suspicious lesions.[3,4] By integrating EIS into flexible surgical instruments such as endoscopes, bronchoscopes, and catheters, a more precise

C. C. Nguyen, J. Davies, T. T. Hoang, E. Nicotra, H. A. Tran, B. Sharma, K. Zhu, P. T. Phan, A. Ji, J. Wan, J. Rnjak-Kovacina, N. H. Lovell, T. N. Do
Graduate School of Biomedical Engineering
Faculty of Engineering
and Tyree Institute of Health Engineering (IHealthE)
UNSW Sydney
Kensington Campus, Sydney, NSW 2052, Australia
E-mail: tn.do@unsw.edu.au

A. Ashok, T. B. Dang, H.-P. Phan
School of Mechanical and Manufacturing Engineering
Faculty of Engineering
UNSW Sydney
Kensington Campus, Sydney, NSW 2052, Australia

A. Ehteda, O. Vittorio
School of Biomedical Sciences
Faculty of Medicine
UNSW Sydney
Kensington Campus, Sydney, NSW 2052, Australia

The ORCID identification number(s) for the author(s) of this article can be found under https://doi.org/10.1002/adhm.202404623

DOI: 10.1002/adhm.202404623

measurement can be achieved. The presence or absence of cancerous cells within suspicious regions can be verified after initial identification through imaging methods. With this method, complex procedures such as biopsies may be eliminated.[4] To bring the onboard metal electrode to the internal organs, surgical instruments with simple, high degrees-of-freedom (DOFs), and precise tip control methods are highly desired. In addition, these instruments should ideally possess high flexibility with miniaturized diameters and multi-functional capability for safe, fast, and successful operations.[5,6] These requirements for surgical tools are even more demanding in microsurgeries.[7,8] This originates from the fact that poor tip control with imprecise motions could lead to unexpected tissue damage and complications during and post-surgery.[9] To achieve such high accuracy, flexible surgical tools should be equipped with tremor filtering mechanisms for eliminating or mitigating the physiologic vibrations (i.e., physical tremors) induced by the surgeons during the operation.[10,11] To promote wound healing post-surgery or regenerative therapies, in situ, biomaterial injection and 3D printing of bioink incorporating living cells on target areas within the human body via minimally invasive delivery have emerged as an innovative solution.[12–16] However, to the best of our knowledge, few, if any, flexible surgical systems can perform in situ cancer detection, surgical ablation, and in situ 3D bioprinting via minimally invasive delivery.

Current advancements in minimally invasive surgery (MIS) have led to the development of innovative teleoperated surgical robotic systems (TSRSs) with the potential to revolutionize complex surgical procedures. Despite these promising strides, significant challenges remain, particularly in the areas of control and actuation methods for TSRSs, limiting their full potential in multifunctional surgical applications.[5] Teleoperation allows surgeons to work away from the radiation source required for real-time imaging during operations.[17,18] TSRSs are equipped with advanced surgical instruments that provide surgeons with enhanced dexterity and precision beyond what is possible with human hands alone. This capability holds significant promise for a wide range of medical applications throughout the human body, improving the efficacy and safety of complex surgical procedures.[19] Compared to conventional techniques, TSRSs enhance safety, accuracy, and speed in both diagnostic and surgical procedures. These improvements contribute to better patient outcomes by reducing surgical risks, minimizing recovery times, and increasing the overall effectiveness of treatments.[20] Several concepts of TSRSs have recently been commercialized with FDA approval, offering a wide range of therapeutic and diagnostic procedures. For example, the Flex robotic system (Medrobotics Corp., MA, USA) was developed for neck surgery and endoscopy,[21] the Ion endoluminal system (Intuitive Surgical, Inc., Sunnyvale, CA) was tailored for bronchoscopy,[22] and the CorPath GRX system (Siemens Healthcare GmbH, Erlangen, Germany) was employed for interventional cardiology.[23] Despite advances, these systems often have limitations primarily owing to the rigidity and complexity of their surgical instruments. For instance, they mostly use tendon-driven actuation with pairs of antagonistic wires which are associated with high friction, non-linear hysteresis, force loss, and difficulty in miniaturization.[24,25] In addition, they require a complex control system including electronic components, motors, and a series of mechanical parts such as gears, pulleys, belts, and linear sliders. These components inherently lead to signal delays and degradation,[26] system complications,[27] and high costs. To overcome these problems associated with tendon-driven actuation, magnetic composites (e.g., PDMS + NdFeB) controlled by magnetic fields have been proposed.[16,24,28] These flexible robots could provide advanced navigation abilities by accessing the deep cerebral vasculature with submillimeter sizes. They, however, require a bulky magnetic field generator, moving around or underneath the patient bed, causing complications, as well as not being MRI-compatible. Fluidic-driven actuators[9,25,29,30] are also great candidate to deal with the remnant problems of tendon-driven and magnetic actuators because they offer high aspect ratios, flexibility, less friction, and miniaturized scale. Nonetheless, they are often associated with rigid pressure sources including compressors, electrical pumps/motors, syringes/pistons, valves, and complicated control systems. Numerous studies have proposed solutions to this problem. However, the attempts have not been greatly successful due to several limitations including the generated pressure being low,[31–33] the need for high-voltage sources,[34,35] the overall bulkiness of the technology, and its rigidity.[36–38]

Recently, TSRSs with multifunctional surgical instruments have emerged as an important step in further development toward a more mature and adaptable MIS technique. For instance, Lee et al. introduced a multifunctional endoscope-based interventional system offering a closed-loop solution for colon cancer treatment comprising accurate detection, delineation, and rapid targeted therapy of colon cancer and precancerous lesions.[4] Given the integration of transparent bioelectronics with theranostic nanoparticles, this system enables optical fluorescence-based mapping, electrical impedance, pH sensing, contact/temperature monitoring, radiofrequency (RF) ablation, and localized photo/chemotherapy.[39–42] Despite great advancements, this system uses a conventional actuation (i.e., a tendon-driven mechanism) involving the abovementioned limitations and being restricted to applications in the colon. Additionally, microsurgery and tissue and organ damage treatment are challenges for this system. In an attempt to provide in situ bioprinting for repairing tissue injury after surgical operations, Thai et al.[15] introduced a multifunctional and flexible 3D bioprinter with six DOFs to produce endoscopic procedures and deliver multilayered biomaterials to speed up the healing process of the damaged tissue. However, this system involves many rigid parts with a relatively large diameter (20 mm) and lacks sensing capabilities, limiting its widespread adoption. More recently, Rogatinsky et al.[25] proposed a millimeter-scale soft robotic platform for cardiac interventions with multiple functions. It can deploy and self-stabilize at the entrance to the heart, guide existing interventional tools, and conduct reconstructive procedures inside the right atrium (RA) of the heart. Despite advances, this system also lacks feedback information (i.e., no sensing abilities), and has a large diameter of 8 mm limiting its applications to the RA. The three multifunctional platforms mentioned above require complex control systems that integrate multiple motors and electronic components, which may increase risks and complications. Furthermore, these instruments often require reconfiguration

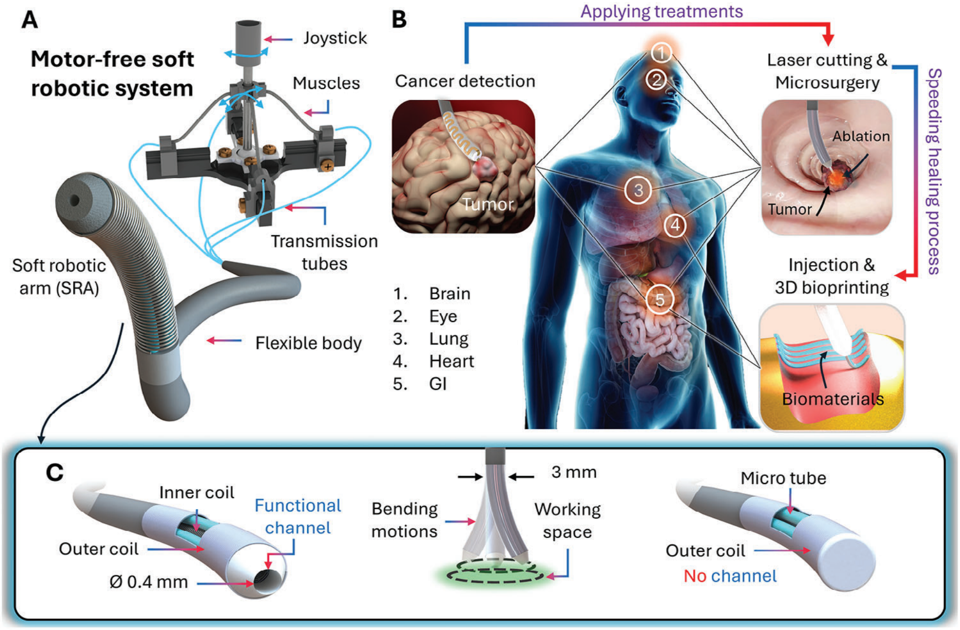

Figure 1. Schematic illustration of the mfSRS and applications: A) Design overview of the mfSRS including a joystick controller and a SRA. This system is built with an advanced structure developed from the SFSA. B) Potential applications of the system across the human body (e.g., inside the brain, eyes, lungs, heart, and GI tract) include cancer detection, laser/ablation microsurgery, and biomaterial 3D printing and injection. C) Designs of two SRA versions including a functional-channeled SRA and a non-channeled SRA. Some images are used under license from stock.adobe.com.

to accommodate new functionalities, potentially limiting their widespread adoption. Consequently, there is a strong demand for a simpler platform that combines essential capabilities with a compact design, enabling a broader range of medical applications within a single system.

To address these challenges, this paper introduces a novel motor-free soft robotic system (mfSRS), which is driven hydraulically and designed for portability. This system serves as a simple, cost-effective platform that delivers high accuracy for MIS. It leverages recent advancements in the design and theoretical framework of the soft fibrous syringe architecture (SFSA) to provide enhanced performance and versatility in surgical applications.[43] The proposed system incorporates multifunctional tools designed for cancer detection, surgical procedures, and in situ 3D printing of biomaterials. Central to this system are two newly developed miniature soft robotic arms (SRAs)–one with a functional channel and one without–that act as essential instruments controlled by an innovative master controller (**Figure 1A**). These SRAs serve as flexible platforms for various functions; for example, by integrating microelectrodes, they can be adapted for tasks such as detection and ablation. The system's precise and stable motion control makes it especially suitable for microsurgical applications. Demonstrated procedures include RF for microsurgery, 3D printing and injection of biomaterials for wound healing, and electrical impedance measurements for supporting cancer detection. These capabilities have been validated through ex vivo and in vitro experiments (see Note S1, Supporting Information). Overall, this mfSRS shows great promise as a comprehensive and adaptable solution for MIS across various parts of the body, including the brain, eyes, lungs, blood vessels, heart, and GI system (Figure 1B).

2. Results

2.1. System Design and Characterization

2.1.1. Design and Working Principle of the mfSRS

Two fundamental configurations for the SRA are proposed in this study (Figure 1C). Both SRAs feature 3-DOFs with four fluid chambers (i.e., silicone microtubes) and a fiber-reinforced layer (i.e., helical coils) with original dimensions of Ø3 × 12.5 mm. One of them possesses a hollow channel while the other does not. The former SRA with a functional channel diameter of Ø0.4 mm was developed to deliver biomaterials (e.g., hydrogels) for in situ 3D bioprinting and biomaterial injection for tissue regeneration purposes (see Figure 7). With this hollow channel, an optical fiber can be inserted into this channel to transfer surgical energy (e.g., laser[9]) for cutting or functional lights for biomaterial curing.[44] The latter, non-channeled SRA integrates microelectrodes to enable multifunctionality. For instance, Au/PI thin films can be incorporated to monitor impedance differences between abnormal tissues and the surrounding environments, supporting cancer detection efforts[4] (Figure 4). Additionally, an ablation electrode can be integrated into the SRA for ablation procedures[45] (Figure 5). Figure S1 (Supporting Information) (Note S2, Supporting Information) details the fabrication method for these two SRAs.

Once the SRA fabrication was completed, its four fluid chambers were hydraulically connected to four master artificial muscles (**Figure 2A**) to form four SFSAs.[43] These master muscles, made of a rubber tube and a helical coil possessing a diameter of 3 mm, were then assembled in a novel master controller

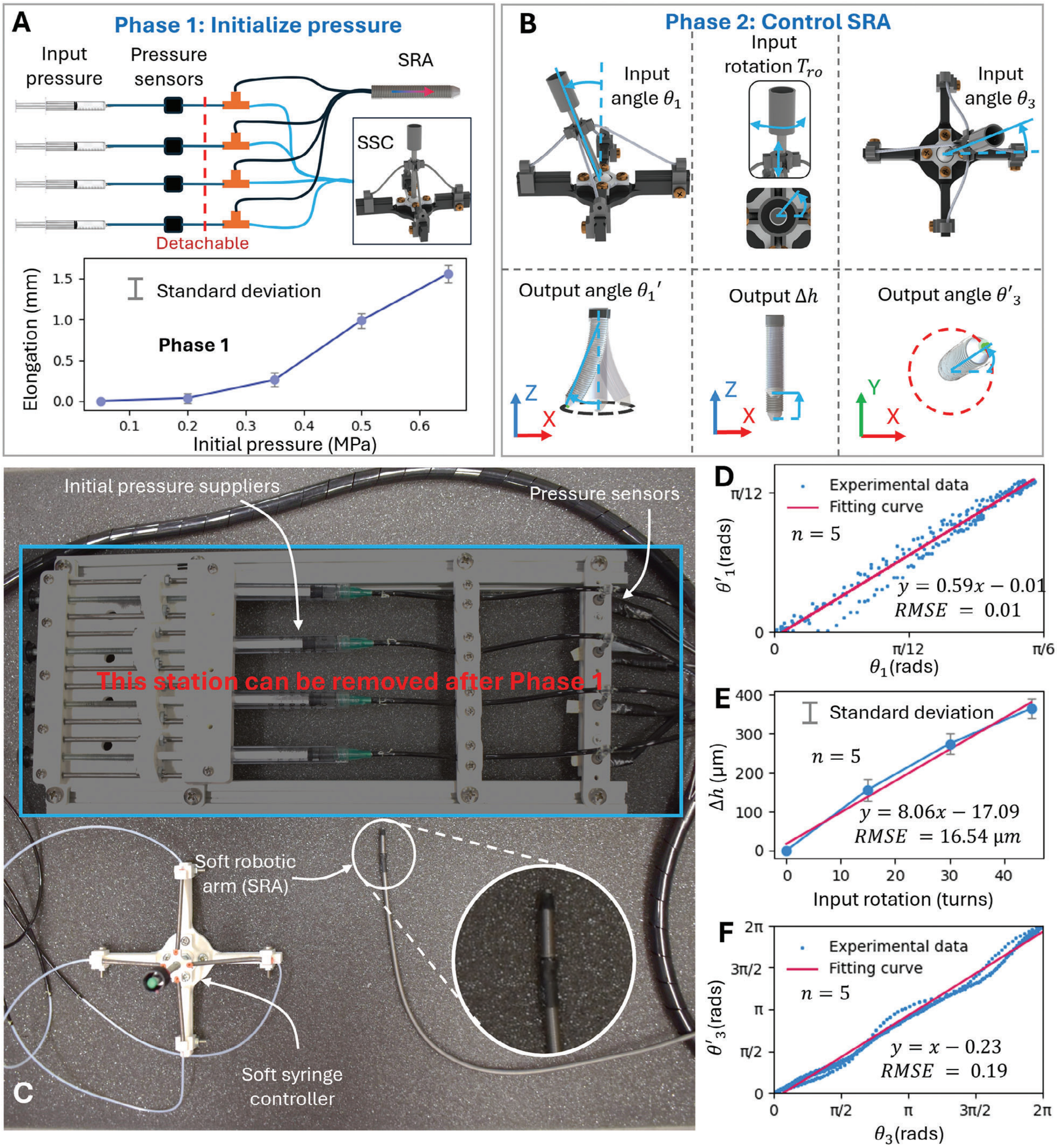

Figure 2. Schematic of the system's working principles with two phases: A) Phase 1: Initial pressure is applied into four fluid chambers of the robot as well as four master muscles to elongate them to the initial lengths, making the workspace of the SRA. Experimental data of Phase 1 with the relationship between the SRA's elongation and the applied pressure. B) Phase 2: Control strategies for three DOFs (θ_1, T_{ro}, θ_3) → (θ'_1, Δh, θ'_3) of the system in the XZ and XY planes. C) The actual prototype of the system includes the SRA, the master controller, and a station storing syringes for initial pressure in Phase 1 and external pressure sensors for system characterizations. D–F) The experimental results of Phase 2 for system characterizations of each DOF with fitting curves and computed root-mean-square errors (RMSE).

(Figure S2, Supporting Information). This master device incorporates a joystick-like structure, allowing the operator to either bend or rotate the joystick around its central point–the ball joint. Fabrication details of this master controller can be found in Note S2 (Supporting Information). Based on the theory of the SFSA, the bending motions of the SRAs can be controlled by the length of these master muscles. Specifically, the working principle of the mfSRS consists of two phases: Phase 1–Initializing pressure in four SFSAs to elongate both the SRA and the master muscles (Figure 2A), generating the workspace of the device;

Phase 2–Modifying the length of the master muscles (by manipulating the joystick as shown Figure 2B) to change the inner pressure of the SFSAs (Figure S2B, Supporting Information), thus bending the SRA.

Figure 2C shows the prototype of the mfSRS, which includes a station equipped with initial pressure suppliers and external pressure sensors, positioned alongside the master controller and the SRA. It is worth noting that this station can be detached after completing the initial phase and system characterization. This design provides three DOFs and enables direct 1-to-1 motion mapping between the master controller and the SRA. Figure 2B presents the control strategies for the three DOFs including bending along the X- and Y-axis $(\theta_1, \theta_3) \rightarrow (\theta'_1, \theta'_3)$ and translating along the Z-axis $T_{ro} \rightarrow \Delta h$. Compared to the soft robotic catheter system presented in previous work,[43] this new device allows a more uniform and compact design. This has been achieved by replacing the outer sheath, made of heat shrink, with an outer helical coil, and eliminating the helical coils from the artificial muscles (Figure S1A, Supporting Information). Specifically, the previous device possessed three main components: four silicone rubber tubes, four helical coils, and a heat-shrink outer sheath. At the same time, the new design requires only four silicone rubber tubes and a single outer helical coil (Table S2, Supporting Information). Notably, although a fifth silicone tube and a small helical coil for the functional lumen were incorporated into the device to form the hollow-channeled SRA, uniformity, and compactness were maintained (Figure S1B, Supporting Information). Additionally, more precise Z-axis control for the SRA allows operators to adjust the nozzle's height (i.e., the SRA's tip) with greater resolution.

2.1.2. SRA Motion Comparisons

From two fundamental SRAs given in the previous section, four different instruments (**Figure 3**A,B) were constructed and investigated in this study. Given the diverse construction of these instruments, it is necessary to examine the effects of the structures and embedded components on the SRA' bending motions. To obtain this, we conducted an experiment where a single input pressure was induced in one fluid chamber of each SRA to make it bend in a 2D plane. Meanwhile, the movements of the SRA's tip in a 2D plane were recorded (Figure 3C). It is noted that one of the main focuses of this study is to validate the integration of flexible electronics into a SRA to support tumor detection. Thus, we aimed to select an electrode design that is both simple and effective, ensuring minimal impact on the soft arm's bending motion. Based on our analysis, serpentine, and spiral electrode structures are the most suitable choices for this application due to their simplicity and efficiency. Through experimental comparisons of the bending motions facilitated by these two structures, we found that the serpentine structure enables significantly greater motion than the commonly used spiral structure (Figure S3C, Supporting Information). Additionally, the serpentine structure offers distinct advantages, including superior flexibility, reduced stress concentration, and efficient signal transmission, reinforcing its suitability for this application. Therefore, the serpentine structure has been employed as the optimal design for this application.

Results shown in Figure 3D–F indicate that the channel-attached sensing electrodes and the inserted optical fiber reduced the bending motions of the SRAs by ≈35%. However, these additional components greatly reduced the hysteresis exhibited by the non-channeled SRA (Figure S6B, Supporting Information). Figure 3E reveals that the optical fiber has the most pronounced effect on the motion of the SRAs. This can be attributed to the non-stretchable material properties of the optical fiber and the additional stiffness it imparts to the SRA. Therefore, this instrument was selected for use in characterizing the system in the subsequent section.

2.1.3. Characterization of the mfSRS

To evaluate the system's motion control capabilities, experiments were conducted across both phases. Experimental details can be found in Section 4. The results shown in Figure 2A (bottom) reveal a nearly cubic relationship between the SRA's initial elongation and the initial pressure, with a maximum elongation of ≈1.5 mm (≈12.5% of the initial length) occurring at an initial pressure slightly exceeding 0.6 MPa. In Phase 2, each DOF was characterized separately as shown in Figure 2D–F with computed curve-fitting equations and RMSEs. It was observed that the relationships between inputs and outputs were nearly linear with small RMSEs of ≈0.01 rads compared to their range for the DOF θ_1 and θ'_1, 16.54 µm for the DOF T_{ro} and Δh, and 0.19 rads for the DOF θ_3 and θ'_3. Furthermore, Figure S5 (Supporting Information) presents the recorded pressure changes of the four SFSAs and the data points of the SRA's end-effector in the XZ plane with a parabolic fitting curve and RMSE of 0.01 mm for the first DOF θ_1 and θ'_1.

It is worth noting that the combination of the screw mechanism–converting rotational motion T_{ro} into linear motion Δh–at the master controller and the SFSA established an ultra-high resolution in controlling the Z-axis of the system. Specifically, the inner pressure of the four hydraulic channels dropped from ≈0.6 to just under 0.4 MPa after 45 turns of the master DOF T_{ro} (Figure S2B, Supporting Information), lifting the SRA tip by a distance of ≈400 µm, creating a significantly high resolution of roughly 9 µm per turn for control of the Z-axis. This unique capability of the system offers a great solution for microsurgical tasks to either create or remove ultrathin layers. In addition, this control resolution can be simply modified by either changing the initial pressure of the SFSA or the screw pitch of the master device, or both. The workspace of this system is defined by the initial pressure (or energy) stored in its actuators as the nature of the SFSA, meaning there are motion limits that cannot be exceeded. This greatly helps the system meet the rigorous requirements of MIS safety by avoiding overreaching into regions of the healthy tissue, highlighting the novelty of mfSRS as there are few if any systems possessing this ability. The limited workspace may, however, restrict its application to small targeted objects. Despite that, the system can be scaled up by simply adjusting the size of its components to accommodate larger targeted objects. It is worth noting that this work represents an advanced step in design and material selection, pushing the boundaries of compactness and achieving the smallest version of the system using the SFSA technology. One typical example is presented in our previous study,[43]

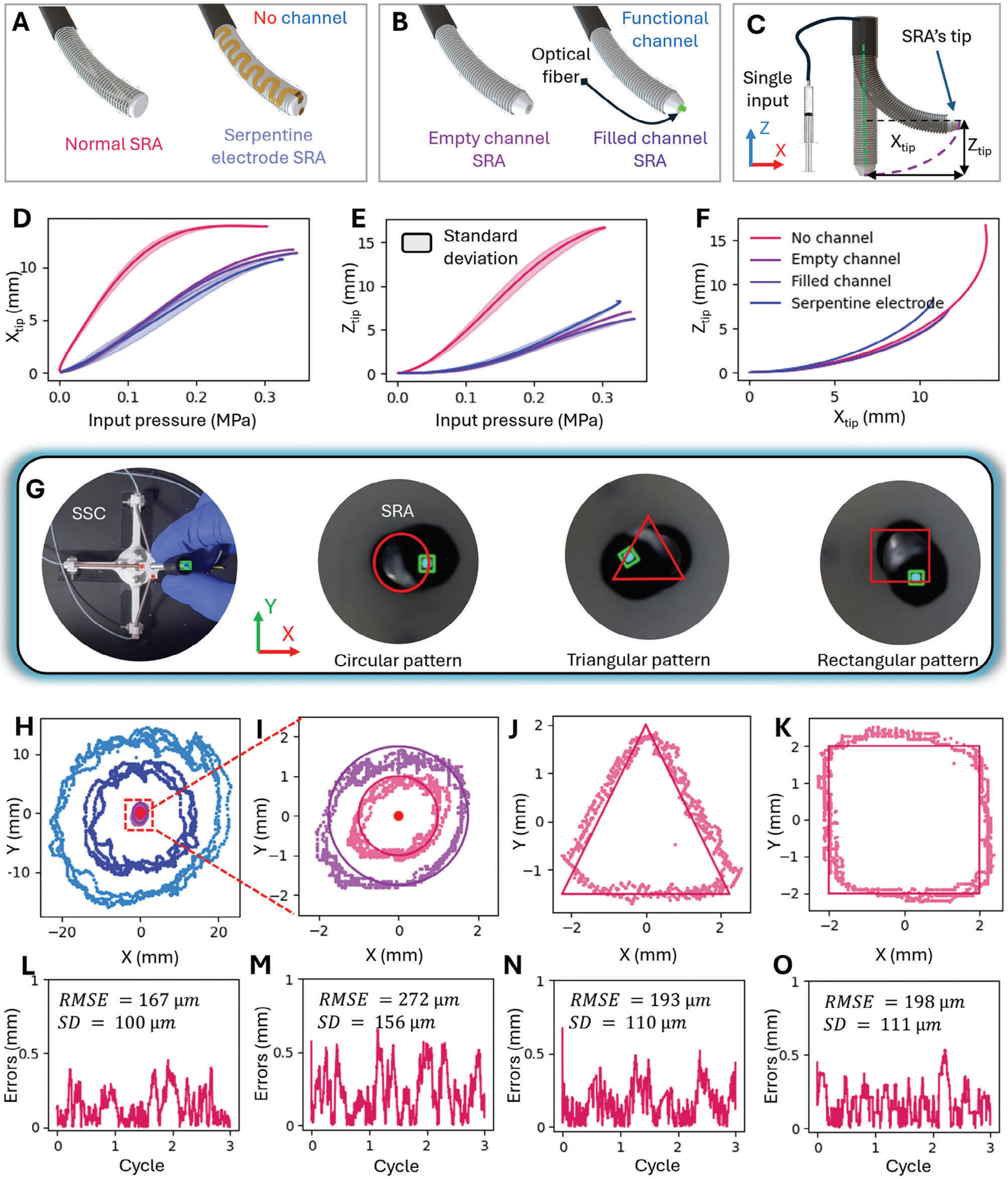

Figure 3. Motion comparisons and micro-operations: A,B) Designs of four miniature instruments: non-channeled SRA, non-channeled SRA with integrated serpentine electrodes, functional-channeled SRA, and functional-channeled SRA with an inserted optical fiber. C) Experimental setup for motion comparisons with a single input pressure. *Results of motion comparisons with the relationship of*: D) SRA's tip along the *X*-axis and corresponding input pressure; E) SRA's tip along the *Z*-axis and the corresponding input pressure; F) SRA's tip in the XZ plane. G) The experimental setup where both SSC's and SRA's motions are captured on the XY plane (top-view camera). H) Input and output data points of the master joystick and the SRA following targeted trajectories of two circles with radii of $R_1 = 1$ mm and $R_2 = 1.75$ mm. I–K) Magnified data points of the SRA's tip following the two circular patterns, a triangular trajectory, and a rectangular trajectory, respectively. L–O) Errors of the data points compared to the targeted trajectories with calculated RMSE and SD for the circular (R_1 and R_2), triangular, and rectangular trajectories, respectively.

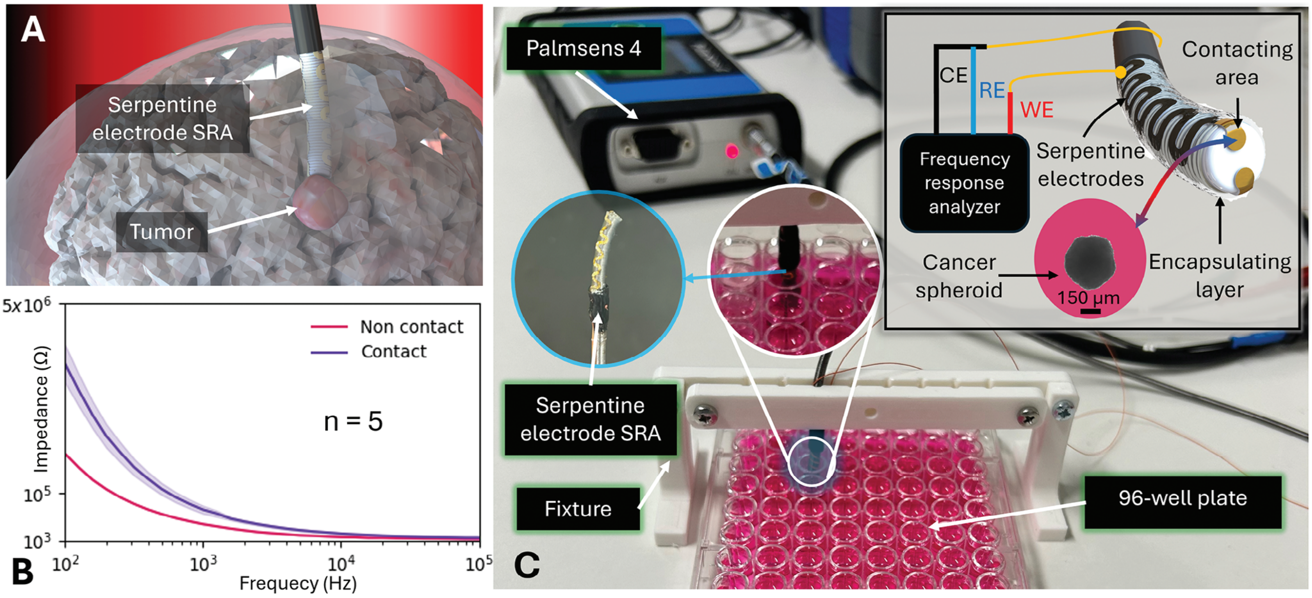

Figure 4. A) Schematic of an exemplary application of the device performing EIS for detecting tumors. B) The results of in vitro impedance measurements. C) Experimental setup of in vitro EIS, where a frequency response analyzer, the non-channeled SRA with integrated serpentine electrodes, and cancer cells (spheroid) are used.

an SRA having an overall diameter of ≈4.5 mm (with an outer sheath made of heat shink) can result in a larger workspace. This scalability and adaptability make the system versatile, ensuring it can address broader surgical needs while maintaining its compact and electricity-free design.

2.1.4. Micro Motion Control

During micro-operational tasks such as laser cutting or RF ablation, the distal SRA is actively maneuvered and ultimately accounts for the overall steering precision of the system. The SRA with an inserted optical fiber was tested to validate its accuracy using a series of exercises that map to predefined patterns including circles with different radii, a triangle, and a rectangle (Figure 3G; Movie S1, Supporting Information). Two cameras (HD Pro Webcam C920, Logitech) were set up at 60 FPS and HD 1080p to capture the input motions of the joystick controller and the output motions of the SRA's tip. The workspace in the XY plane was designated to be a circle radius of 5 mm with a maximum bending angle of 30 degrees in the XZ plane. Figure 3H shows the data points of the input and output motions for the case of the circular patterns. In contrast, Figure 3C–E presents the outputs' magnified data for circular, rectangular, and triangular patterns, respectively. The errors, RSMEs, and standard deviations (SD) were computed for each pattern and presented in Figure 3E–H. Specifically, the RSME for a circle $R_1 = 1$ mm was 167 µm, which was increased to 272 µm for the larger radius circle $R_2 = 1.75$ mm. The RSMEs of the triangle and rectangle were similar at just under 200 µm. Similarly, the calculated SD for each test showed a maximum of only ≈156 µm.

It is worth noting that soft robots controlled by conventional methods (e.g., using DC motors with rigid pressure suppliers) often face challenges due to sudden volume changes in their soft actuation chambers.[15,25,46] This is particularly problematic for steering the robot's tip to track patterns involving sharp turns, such as triangles and rectangles, which can induce snap motions. Despite these challenges, our proposed mfSRS maintains high accuracy (see Figure 3N–O). Furthermore, this proposed system also greatly reduces physical tremors induced by the operator's hand, significantly enhancing the accuracy of the procedure. As discussed above, the RMSEs of the SRA for the cases of two circles were minimal, ≈9 and 6 times smaller than those of the master controller. As illustrated in Figure S7 (Supporting Information), these RMSEs were ≈1.52 and 1.64 mm, respectively.

2.2. In Vitro Impedance Measurements

In this study, we experimented with flexible serpentine electrodes attached to the tip of the SRA composed of a thin Au/PI film for performing EIS to assist in cancer detection (**Figure** 4A). Fabrication of these electrodes is presented in Section 4 while the integration of them into the SRA is detailed in Note S3 (Supporting Information). To validate the device, in vitro contact impedance measurements were performed in a cell medium with spheroids, 3D cultured from U87 glioblastoma cells (detailed in Section 4), selected by diameters ranging from 350 to 500 µm. By constructing a two-electrode system with an electrode spacing of 0.8 mm connected to a frequency response analyzer (PalmSens4, Palmsens, Houten, Netherlands), this configuration was employed to measure the change in contact impedance on a healthy spheroid. The encapsulating layer (Eco-flex 00–10, Smooth-on Inc.,) covers the electrodes along the SRA's body, leaving only the top surface exposed to the environment. Figure 4C shows the actual setup of this experiment, where the SRA was inserted into the wells of a round-bottom 96-well plate and stabilized by a 3D printed fixture to ensure proper contact between the working serpentine electrode and the spheroid. Figure 4B depicts the change in impedance observed through Au-coated flexible PI electrodes, where an increase in impedance upon contact with the spheroid's surface. The maximum discrepancy is observed at a frequency of 100 Hz, where the impedance of the medium is ≈376 kΩ, while the impedance in the spheroid-involved step is ≈183 kΩ. The change in impedance before and following contact with the spheroid suspended in liquid media is primarily attributable to the regulated free ion gradient at the cell membrane, which functions as a selective barrier. This lipid bilayer exhibits high insulating properties and impedes the flow of electrical current, thereby contributing significantly to the overall impedance by causing the membrane to behave as a capacitor, accumulating charge rather than permitting unrestricted ion movement, thus increasing the impedance. This finding demonstrates the device's capability to detect differences in impedance, highlighting its potential for supporting the identification of cancerous tumors within their environment.

2.3. Minimally Invasive RF Ablation

Section 2.1 has highlighted the mfSRS's capabilities in providing high-precision motion of the SRA's tip. To evaluate the feasibility of this telemanipulation of the system for microsurgery, a minimally invasive RF ablation test was conducted (**Figure 5**; Movie S2, Supporting Information). The non-channeled SRA with a micro tip (i.e., an ablation electrode) was employed–manufactured from a 30 GA needle (Figure S3A, Supporting Information). The SRA and a miniature scope (Ø 1.66 mm–MISUMI Electronics Corp, Taiwan) were inserted into a 3D printed chamber through small holes with a diameter of less than 5 mm, simulating a laparoscopic MIS (Figure S8, Supporting Information). A piece of fresh porcine tissue was placed into the chamber and in contact with the earth plate of the high-frequency electrosurgical unit (LED Surtron 120, StarkMed Pty Ltd., Australia). Blue food dye was used to outline a rectangular intended site (≈3.5 × 3.5 mm) for the ablation.

To implement the ablation procedure, the SRA was first positioned over the marked site (Figure 5B,F). The cutting tip was then moved down along the Z-axis (by the second DOF $T_{ro} \rightarrow \Delta h$) until in contact with the porcine tissue (Figure 5C,G). The electrosurgical unit's cut output power was adjusted to 100 W. The operator then activated the foot pedal of the electrosurgical unit, initiating the ablation process. The procedure began at the edges of the marked area, gradually moving inward to remove the interior tissue (Figure 5D,H). After the ablation was completed, the cutting tip was lifted to a safe distance from the tissue before being pulled out of the operation site (Figure 5E,I). The entire procedure was manipulated and monitored by the operator through the master controller and the visual feedback provided by the miniature scope (Movie S2, Supporting Information). Figure 5J–L shows the status of the operation site before and after the procedure, and a close-up view of the ablated area, respectively. These results demonstrate that our proposed mfSRS is capable of performing highly accurate ablations on small, targeted areas, as small[7] or smaller[9] than those achieved by published robotic systems for high-precision MIS. Unlike existing systems which often require complex and expensive electrical components or complicated systems, our mfSRS operates without using such components. Additionally, the mfSRS's ability to provide precise control over the cutting tip allows for the removal of very thin layers of tissue, ≈0.1 mm in this example, further highlighting its advanced capabilities.

2.4. Minimally Invasive In Situ 3D Bioprinting and Biomaterial Injection

In situ 3D bioprinting refers to a method in which bioinks are directly printed at a defect site in a clinical setting to repair living tissues or deliver therapies for wound healing. While most current in situ 3D bioprinting technologies focus on repairing tissues such as skin, bone, and cartilage, the digestive and genital tracts are excellent candidates for such technologies due to their easy accessibility via minimally invasive procedures.[14] When it comes to healing internal tissues, the 3D printing approach offers the potential for a safer and simpler solution compared to conventional surgical sutures.[15] Unfortunately, existing robotic platforms for minimally invasive 3D bioprinting are complicated and costly due to the need for many mechatronic components. Therefore, the SRA with the functional channel has been developed in this paper to address these challenges. To demonstrate the capability of the proposed mfSRS in performing minimally invasive in situ 3D printing, a series of experiments including laboratory tests as well as minimally invasive ex vivo trials were carried out (**Figures 6** and **7**).

Figure 6A illustrates the printing process of a circular pattern with two stacked layers using a gel composite, which was made from cationic polymers, silicone, alcohol, and olive oil. Specifically, the mfSRS initially prints the circular edge and then fills in the first layer. After moving the nozzle upward, the system completes the second layer. In addition, demonstrations of the printing process for rectangular and triangular patterns have also been carried out and shown in Figure 6C,D, respectively. We repeated the printing process in three iterations for each pattern. Figure 6D (left) presents the results of the printed edge and two layers, in which the printed edge has a width of 0.5 mm, which is only 0.1 mm wider than the diameter of the functional channel. Additionally, Figure 6D (right) presents the printed results from the repetitions, analyzed using a radial sweeping method to calculate their errors compared to the defined curves. As shown in Figure 6E, the errors for the circular pattern are the smallest compared to those for the rectangular and triangular patterns. This is likely due to the inherent challenges of printing shapes with sharp corners, as evident in the pronounced error spikes corresponding to the four corners of the rectangle and the three corners of the triangle.

Applying pressure to the functional channel during the printing process can have a significant impact on the bending motion of the SRA. Therefore, determining the safe pressure range to estimate the maximum viscosity of the printing materials for a given volumetric flow rate (VFR) is essential. To address this, we have conducted experiments to characterize the printing pressure. The experimental details are shown in Figure 6F and Section 4 of this study. Briefly, we blocked the channel outlet, applied pressures in 0.05 MPa increments, and tracked the bending motion of the SRA (Figure 6F; Movie S3, Supporting

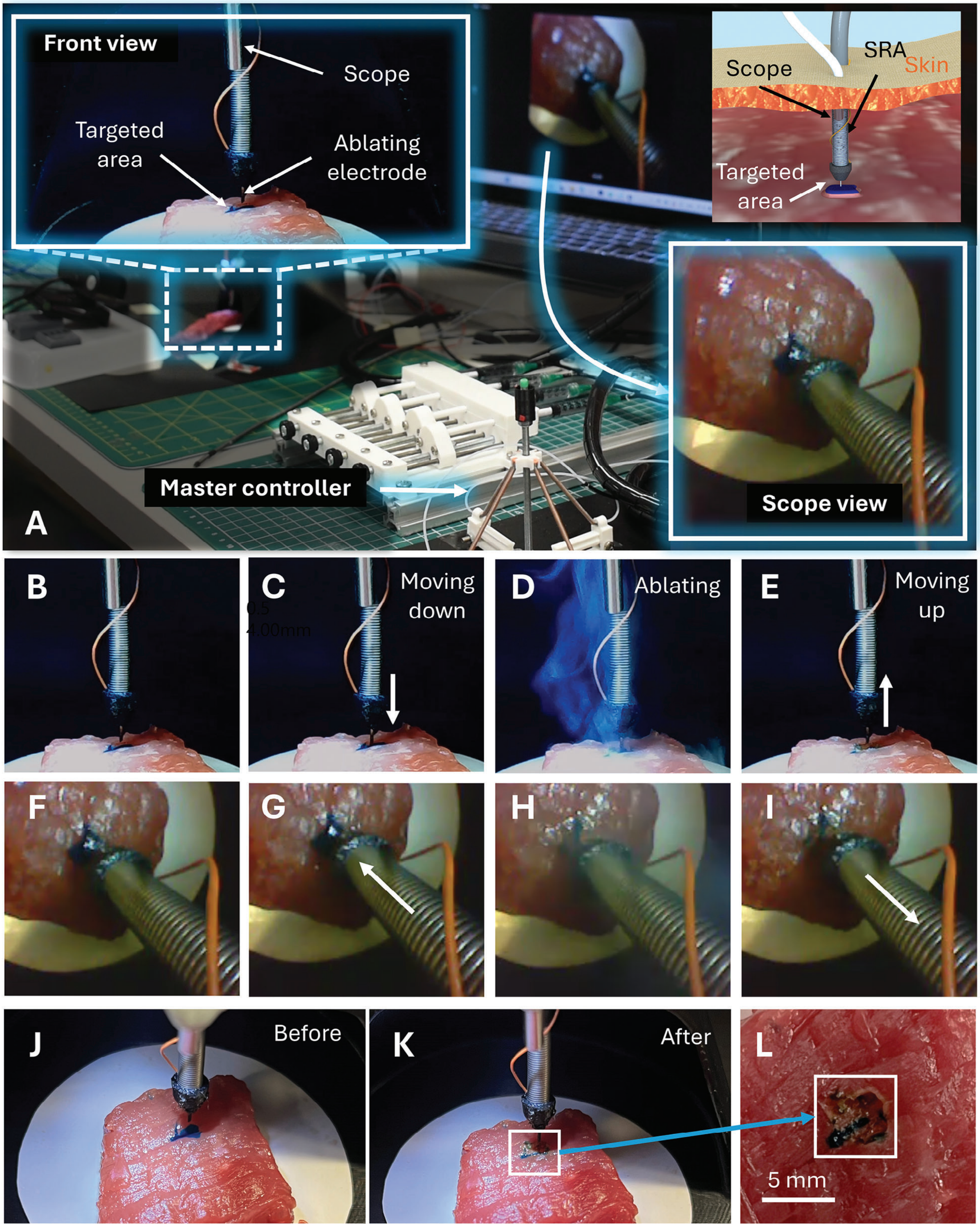

Figure 5. Minimally invasive RF ablation (Movie S2, Supporting Information): A) Experimental setup includes front and scope camera views capturing the motions of the ablating-electrode-integrated SRA controlled by the master controller. *The ablation process from front/scope views*: B,F) the SRA is positioned to the working site; C,G) the SRA is moved down to be in contact with the tissue; D,H) RF energy is transferred to generate the ablation while the SRA is steered to remove the targeted area; E,I) the SRA is moved up to complete the procedure. J) Image of the experimental site showing the position of the SRA and the aimed area. K,L) The results of the RF ablation zoomed in to the ablated tissue site.

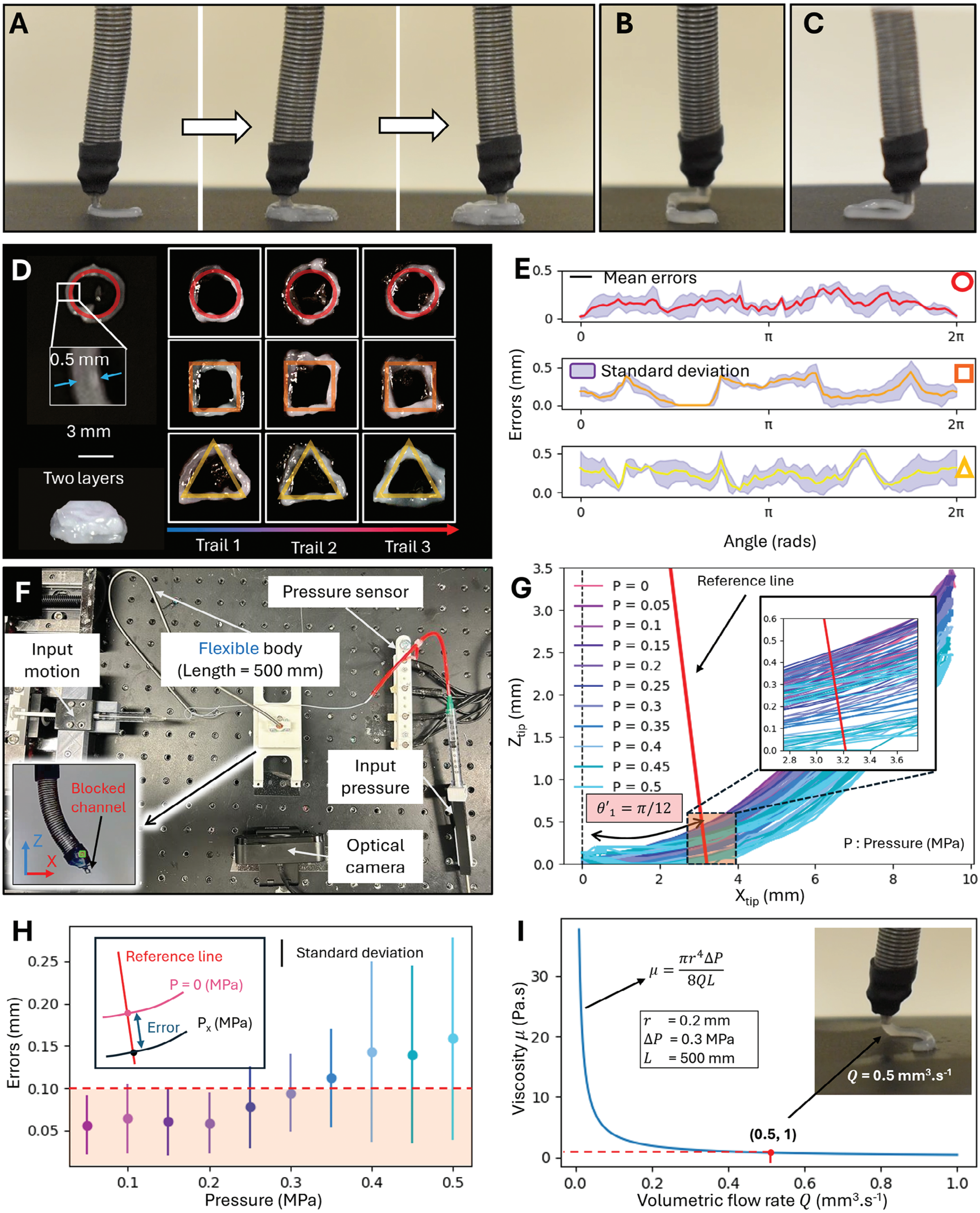

Figure 6. Laboratory bioprinting demonstrations and printing pressure characterizations: A) Laboratory bioprinting process of a circle pattern with two layers (Movie S3, Supporting Information). B,C) Laboratory bioprinting test of rectangular and triangular patterns, respectively. D) Results of the bioprinting process for circular patterns and repeated trials across three iterations for each pattern. E) Computed errors of the printed results compared to the defined curves. F) Experimental setup for characterizations of the printing pressure through the channel where the channel outlet is sealed. G) Results of the SRA's bending motion corresponding to each pressure applied to the channel and a definition of the reference line. H) Computed errors of the SRA's bending motion corresponding to each pressure applied to the channel. I) Relationship of maximum material viscosity μ and the desired VFR Q with a typical example for $Q = 0.5$ mm^3 s^{-1}.

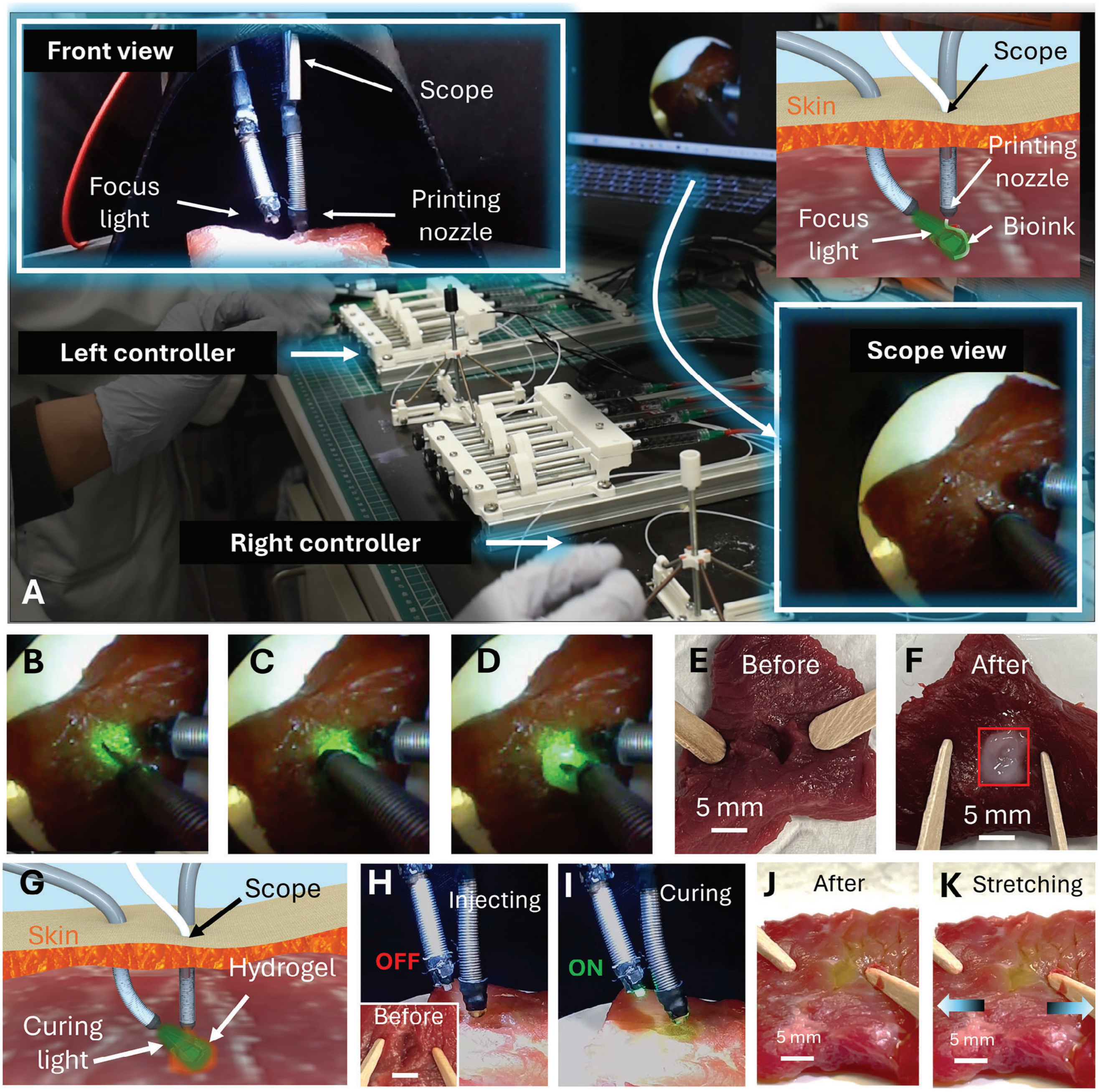

Figure 7. Demonstrations of minimally invasive bioprinting and biomaterial injecting: A) Experimental setup of ex vivo 3D printing including front and scope camera views capturing the motions of the flexible printing nozzle and the focus light controlled by the right and left master controller, respectively (Movie S4, Supporting Information). B–D) The process of the ex vivo 3D printing. E,F) Photos of the wound before and after the printing procedure. G) Schematic of biomaterial injecting procedure, in which two SRAs including the injecting nozzle and the curing light are used. H) The biomaterials (silk hydrogel precursor) start being injected, and the curing light is off. Photo of the wound before the printing procedure. I) The curing light is on and the SRA with light is following the injecting SRA. J) Photo of the wound after the printing procedure. K) Stretching test of the wound after the printing procedure (Movie S5, Supporting Information).

Information). As expected, there was a reduction in the bending motion of the SRA once pressure increased (Figure 6G). To quantify this, we defined a reference line with a slope corresponding to an angle of $\pi/12$ radians with the Z-axis–the working range of the angle $\theta_1{}'$ on the XZ plane (Figure 2D). This line intersects the bending curve of the SRA's motions at certain points, which we termed "considered points." Additionally, the origin point was determined as the intersection of the reference line and the bending curve when no pressure was applied to the channel. For each channel pressure, we calculated the error in the SRA's motion as the distance between the considered point and the origin point. As shown in Figure 6H, when the applied channel pressure is less than or equal to 0.3 MPa, the bending motion of the SRA shows minimal deviation, with a mean error of less than 0.1 mm and a small margin of error of ± 0.05 mm. However, the errors slightly increase when the pressure is higher than this point and reaches a mean error of 0.15 mm at a large range of uncertainty of ± 0.15 mm. Based on these findings, maintaining the channel pressure at or below 0.4 MPa is recommended to minimize impacts on device accuracy. Using the Hagen–Poiseuille equation, we derived the relationship between maximum viscosity and desired VFR of biomaterials, as displayed in Figure 6I. This result provides users with valuable guidance for selecting materials that match their desired printing flow rates. For instance, when printing at a VFR of ≈0.5 mm^3 s^{-1}, a material with a viscosity below 1 Pa·s was selected to ensure optimal performance (Figure 6I).

We also performed minimally invasive 3D printing experiments (Figure 7A) using a similar setup to the previous ablation experiment. To enhance the visibility for this procedure, an additional SRA was employed to provide the focusing light (Light source: green beam–710 USB Star-light, Dinsom, Amazon) delivered through an inserted optical fiber with a diameter of 0.25 mm (AZIMOM PMMA, plastic end glow fiber, Amazon) (Figure S10, Supporting Information). It is worth noting that the light source can be simply changed to meet the requirement of light-curing bioinks such as photocrosslinkable hydrogels.[44,47] While the main operator used left and right master controllers to manipulate the two SRAs, the second operator managed the light source mode (on/off) and the speed of material feeding. Figure 7B–D presents the printing process recorded by the miniature camera (scope view), where a layer of the gel composite was printed to cover the targeted wound (Movie S4, Supporting Information). The wound status before and after the printing process is illustrated in Figure 7E,F.

Finally, we further demonstrated the ability of the mfSRS to perform wound healing by injecting a biomaterial–silk hydrogel precursor (Figure 7G).[44] The preparation of this biomaterial has been detailed in Section 4. Since this material is liquid-based and cured by visible light into a hydrogel, we used the same light source presented in Section 2.3 and focused on controlling the light-delivering SRA. Similar to minimally invasive 3D printing, two operators are required to operate this procedure; one operator controls the motion of the two SRAs while the other operator takes care of the speed of material injection and the light source mode. Figure 7H,I shows the material injecting and curing process of this experiment, where the material was first injected into the targeted wound and the curing light was turned on and steered to cure all areas around the wound. Figure 7H presents the wound status before the procedure, while the wound status after the procedure has been depicted in Figure 7J. The material was rapidly cured into an elastic hydrogel in the wound site and stretching of the tissue demonstrated that the material adhered well to the irregular wound area and closed and stabilized the injury (Figure 7K). This photoinitiated crosslinking reaction results in the formation of covalent di-tyrosine bonds in proteins including silk[48] and has been demonstrated to crosslink protein-based biomaterials to native tissue,[49] like what is observed here. This points to the utility of the mfSRS in delivering biomaterials or tissue-engineered therapies to complex and irregular wounds in a controlled manner.

3. Discussion and Conclusion

By leveraging advancements of the simple yet effective theoretical framework from the SFSAs,[43] we established a new teleoperated surgical robotic platform with two fundamental surgical robotic instruments (the functional-channeled and non-channeled SRAs) for a wide range of MIS applications across the human body. Specifically, based on two fundamental SRAs, four robotic instruments with integrated microelectrodes and optical fiber were designed to provide comprehensive medical functions, addressing the current limitations of TSRSs in MIS. An in-depth review of the current technical challenges faced by flexible robotic systems for MIS, along with a comparison to our proposed system, is provided in Note S1 (Supporting Information) and summarized in Table S1 (Supporting Information).

First, the non-channeled SRA, integrated with an ablation electrode, was successfully validated through an ex vivo micro RF ablation procedure targeting a small area (3.5 × 3.5 mm^2), which is as small as or smaller compared to previous studies.[7,9] Unlike previous efforts that used complicated control systems with neural network models,[9] electrothermal actuation (which can cause tissue damage),[7] or expensive piezoelectric actuators and complex origami structures,[50] our proposed system can achieve highly precise manipulation (mean errors < 300 µm) (see Subsection 2.1.4) without the need for any expensive mechatronic components. Furthermore, it can substantially reduce physical tremors[51] caused by the operator's hands, attenuating them by a factor of nine in a case study presented in this paper (see Subsection 2.1.4). However, the positioning error of less than 300 µm may not be suitable for ultra-high precision, such as some laser ablation surgeries[7] or vitro-retinal eye surgery,[52] which may require a higher level of precision (e.g., less than 50 µm) to avoid damage to adjacent healthy tissues. This limitation is a result of the current manually driven nature of the system, which may not achieve the precision required for such sensitive procedures. The reduction of physical tremors in this system (i.e., the system's accuracy) heavily relies on the motion scaling factor (MSF = input motion: output motion), which also impacts the motion range of the system. Therefore, future work will focus on not only improving material properties and system design but also on thoroughly analyzing the application's precision requirements to achieve an optimal balance between MSF and the system's motion range.

Second, in situ, biomaterial 3D printing and injecting for inner wound healing was performed by two functional-channeled SRAs with a micro-optical fiber integrated into one of them. The results highlight the potential of the system to either provide a scaffold serving as a housing for in situ tissue regeneration[13] or deliver therapeutic drugs.[53] Compared to previous works that require bulky and intricate components such as magnetic field generators,[16] DC motors,[15] or an on-board electrical circuit,[14] our system is much simpler more cost-effective and even portable. Additionally, this system features a miniature printing head with a diameter of 3 mm which is relatively comparable to other published technologies. The printing pressure was also characterized, with an optimal pressure identified as less than 0.3 MPa to avoid significant impacts on the accuracy of the SRA's motion. Based on this, the material viscosity can be determined for the desired VFRs, providing crucial guidance for material selection in these applications (Figure 6I). Last, but not least, the non-channeled SRA with attached serpentine microelectrodes was demonstrated by in vitro experiments to precisely differentiate the spheroids (cancer cells) from their environment (medium) through electrochemical impedance measurements, potentially supporting cancer detection procedures in MIS.[4]

Additional components on the device, in effect, significantly increased its stiffness, thereby reducing the robots' motion range (Subsection 2.1.2). This subsequently minimized the system hysteresis itself as evident in Figure S6 (Supporting Information). On top of these four examples of SRAs presented in this study, other combinations and configurations can be also developed based on our mfSRS, for instance, the integration of additional electrodes for temperature[54] and force[55] sensors for monitoring the ablation process. It is worth noting that once the SRA is connected to the master controller to form SFSAs, the workspace of the device will be tied to its initial pressure. Therefore, it may constrain its application to smaller targeted objects. However, the system can be scaled up by simply adjusting the size of its components to accommodate larger targeted objects. With its scalability and adaptability, the system is versatile enough to address a wide range of surgical needs, while maintaining its compact and electricity-free design.

It is worth noting that this paper focuses on the development of multifunctional and scalable devices within a single compact design. Sometimes, tool withdrawals and reinsertions or the use of multiple SRAs are required to perform multiple steps of the procedure. For instance, a task including biomaterial dispensing and light transmitting steps–with an inserted optical fiber–can be operated by either using two SRAs simultaneously (Figure 7H,I) or using a single SRA in two separate steps. These steps involve withdrawing the SRA for cleaning by introducing clean water to remove the residual biomaterial–and then reinserting it with an inserted optical fiber to perform the second step of transmitting light. Although at this stage the second operator is required to get involved with some procedures such as the minimally invasive 3D printing and biomaterial injection, they can be replaced by future work where the speed of material feeding, and the light source mode would be adjusted by the pedals managed by the main operator's foot. The next step is to integrate the SRAs into an endoscope to enable the capability of performing natural orifice transluminal endoscopic surgery (NOTES) without any incisions. Furthermore, both dimensions and stiffness of the SRAs can also be enhanced by future work to improve the accessibility (e.g., scaling down to submillimeter to access small blood vessels[45,56]) and functionality (e.g., adding high force-required tasks like a surgical grasper) of the system. These future improvements would provide great potential for obtaining a portable, low-cost, and multifunctional surgical endoscopic platform with two SRAs controlled by one operator with a compact master console for NOTES.[18]

Currently, the device is not MRI-compatible due to the helical coil being made of stainless steel. This material was selected at this stage as a cost-effective option for prototyping. However, we fully intend to address this limitation in future iterations of the device by replacing the stainless steel with a Nitinol coil, which is a straightforward step.[57] It is worth noting that Nitinol possesses similar mechanical properties but is MRI-compatible, making it a suitable alternative for such applications.[58] In addition, future work will also focus on material optimization, system design, and the incorporation of solutions to mitigate temperature-induced effects. These enhancements will ensure that the device maintains its performance and MRI compatibility in practical applications.

In conclusion, we have introduced a simple, low-cost, and portable platform–the mfSRS–that serves as a fundamental system for a wide range of surgical applications in MIS without the need for any motors or electrical control systems. While high-accuracy RF ablation, in situ 3D printing biomaterial injecting, and in vitro impedance measurements have been demonstrated in this paper, many other procedures for diagnosis and treatments across the human body could be performed using this system. Thus, this approach potentially opens a new direction in the development of the next generation of TSRSs for improving clinical outcomes of MIS.

4. Experimental Section

mfSRS Motion Characterization: In Phase 1, the initial pressure was increased by four pressure suppliers and recorded by external pressure sensors (40PC250G2A, Honeywell, USA) (Figure 2C), while the SRA's tip was tracked by a camera (60 FPS, HD Pro Webcam C920, Logitech Inc., CA). In Phase 2, the master device's end-effector was commanded by an operator to induce motions for the SRA's tip in planes XZ and XY, while they were both measured by the cameras as shown in Figure S4 (Supporting Information) and Figure 3G (the circular pattern). It was noted that the initial pressure was set at 0.6 MPa for Phase 2 and each test was repeated five times (Figure S5, Supporting Information). Image processing with OpenCV was employed to extract the data points.

Printing Pressure Characterization: A single input pressure, driven by a linear motor (Zaber, model X-LRQ150BL-E01, Zaber, Canada) with a sine wave frequency of 0.5 Hz, was continuously applied to a channeled SRA to induce bending motions. While the outlet of the functional channel was sealed, its inlet was connected to a pressure sensor (40PC250G2A, Honeywell, USA) and a 1 mL syringe to manually apply pressure from 0 to 5 MPa with an increment of 0.05 MPa (Figure 6F). The SRA's tip was tracked by a camera (60 FPS, HD Pro Webcam C920, Logitech Inc., CA). Image processing with OpenCV was employed to extract the data points (Figure S9, Supporting Information).

Silk Hydrogel Precursor Preparation: Regenerated silk fibroin solution was prepared as previously published.[44] Briefly, *B.mori* cocoons were cut into small pieces and boiled in 0.02 M sodium carbonate (Sigma–Aldrich) for 30 min to isolate silk fibroin fibers. The silk fibroin fibers were dried and dissolved in 9.3 M LiBr (Sigma–Aldrich) for 3 h at 60 °C, followed by dialysis against MilliQ water in snakeskin tubing (3500 MWCO, Sigma Aldrich) for 3 days to remove LiBr. The obtained solution was centrifuged twice at 7799 rcf for 15 min at 4 °C to collect the regenerated silk fibroin solution. The final concentration of collected silk fibroin solution was calculated using gravimetric analysis, which ranged from 7 to 9% wt/v. The silk fibroin solution was stored at 4 °C and used for 4 weeks. Silk hydrogel precursor was prepared by mixing silk fibroin solution with tris(2,2′-bipyridyl)dichlororuthenium(ii) hexahydrate (Ru) (Sigma–Aldrich) and sodium persulfate (SPS) (Sigma–Aldrich) to get 6% wt v^{-1} silk, 0.5 mM Ru, and 5 mM SPS in the final concentration.

Fabrication of Serpentine Electrodes: The fabrication of electrodes begins with the evaporation of a 10/100 nm thick e-beam Cr/Au film on a 12.5 µm thick polyimide (PI) film, which was procured from Lab Scientific Co., Ltd., Japan. The evaporation was performed by a Temescal FC-2000 system, under a high vacuum of 2×10^{-6} Torr. The obtained thin film was then attached to a thin layer of double-sided tape and mounted onto the sample holder. A laser cutting (DPSS Lasers, Inc., USA) process was performed to achieve the desired design.

Cell Culture Method: Human U87 glioblastoma cells were cultured in Dulbecco's Modified Eagle Medium (DMEM) containing antibiotics/antimycotics and 10% fetal bovine serum (FBS). Immortalized Normal

Human Astrocytes (NHAs) were grown in a 1:1 mixture of DMEM/F12 and Neurobasal medium, supplemented with HEPES, non-essential amino acids, antibiotics/antimycotics, sodium pyruvate, L-glutamine, 10 ng mL^{-1} rhEGF, and 10% FBS. All cells were maintained at 37 °C in a humidified atmosphere with 5% CO_2. For spheroid formation in 3D cultures, 4 × 10^4 U87 cells and 8 × 10^4 NHAs were seeded in 96-well round-bottom, ultra-low attachment plates (Corning). Centrifugation at 300 g for 3 min to induce spheroid formation, and spheroid growth was monitored over 10 days using bright-field microscopy on the IncuCyte S3 system (Sartorius) at 10× magnification (Figure S11, Supporting Information).

Statistical Analysis: The SD in Figures 2A,E 3D–F, and 4B Figure S3C (Supporting Information), and were calculated and plotted using Python with n = 5. The curve fittings with subsequent RMSE in Figure 2E,F and Figure S5C (Supporting Information) were calculated and plotted using polyfit and polival functions in Python with n = 5. The errors in Figure 3L–O and Figure S7B,C (Supporting Information) were calculated using n = 3, while their RMSE and SD were calculated with n = 1500. The mean errors and SD in Figure 6E,H were calculated using n = 3.

Supporting Information

Supporting Information is available from the Wiley Online Library or from the author.

Acknowledgements

C.C.N., T.T.H., and H.A.T. would like to thank the support of the Science and Technology Scholarship Program for Overseas Study for Master's and Ph.D. degrees, VinUniversity, Vingroup, and Vietnam. The authors acknowledge the support from the UNSW Scientia Fellowship Grant (PS46197), the Cancer Institute NSW Career Development Fellowship (PS66730), and the UNSW GRIP Award (PS74064). This study was partly conducted at the Australian National Fabrication Facility, NSW Node, a firm founded under the National Collaborative Research Infrastructure Strategy to offer researchers in Australia with nano- and microfabrication capabilities.

Open access publishing facilitated by University of New South Wales, as part of the Wiley - University of New South Wales agreement via the Council of Australian University Librarians.

Conflict of Interest

The authors declare no conflict of interest.

Data Availability Statement

The data that support the findings of this study are available from the corresponding author upon reasonable request.

Keywords

minimally invasive surgery, motor-free, soft robotic arm, soft robotics, teleoperated systems

Received: November 19, 2024
Revised: February 9, 2025
Published online: February 17, 2025

[1] A. Jemal, F. Bray, M. M. Center, J. Ferlay, E. Ward, D. Forman, *CaCancer J. Clin.* **2011**, *61*, 69.
[2] R. Aggarwal, V. Sounderajah, G. Martin, D. S. Ting, A. Karthikesalingam, D. King, H. Ashrafian, A. Darzi, *NPJ Digit. Med.* **2021**, *4*, 65.
[3] K. T. Nguyen, H. Y. Kim, J.-O. Park, E. Choi, C.-S. Kim, *ACS Sens.* **2022**, *7*, 632.
[4] H. Lee, Y. Lee, C. Song, H. R. Cho, R. Ghaffari, T. K. Choi, K. H. Kim, Y. B. Lee, D. Ling, H. Lee, *Nat. Commun.* **2015**, *6*, 10059.
[5] P. E. Dupont, B. J. Nelson, M. Goldfarb, B. Hannaford, A. Menciassi, M. K. O'Malley, N. Simaan, P. Valdastri, G.-Z. Yang, *Sci. Rob.* **2021**, *6*, eabi8017.
[6] O. M. Omisore, S. Han, J. Xiong, H. Li, Z. Li, L. Wang, *IEEE Trans. Syst. Man. Cybernet. Syst.* **2020**, *52*, 631.
[7] M. E. Abdelaziz, J. Zhao, B. Gil Rosa, H.-T. Lee, D. Simon, K. Vyas, B. Li, H. Koguna, Y. Li, A. A. Demircali, *Sci. Adv.* **2024**, *10*, eadj1984.
[8] Z. He, J. Dai, J. D. L. Ho, H. S. Tong, X. Wang, G. Fang, L. Liang, C. L. Cheung, Z. Guo, H. C. Chang, *Adv. Sci.* **2024**, *11*, 2305495.
[9] G. Fang, M. C. Chow, J. D. Ho, Z. He, K. Wang, T. Ng, J. K. Tsoi, P.-L. Chan, H.-C. Chang, D. T.-M. Chan, *Sci. Rob.* **2021**, *6*, eabg5575.
[10] S. Yim, S. Kim, presented at *2015 IEEE Int. Conf. on Robotics and Automation (ICRA)*, Seattle, WA, USA, July, **2015**.
[11] N. Jang, Y. S. Ihn, N. Choi, G. Gu, J. Jeong, S. Yang, S. Yim, K. Kim, S.-R. Oh, D. Hwang, *IEEE/ASME Trans. Mechatron.* **2020**, *25*, 1933.
[12] M. Samandari, A. Mostafavi, J. Quint, A. Memić, A. Tamayol, *Trends Biotechnol.* **2022**, *40*, 1229.
[13] Y. Yang, Z. Yu, X. Lu, J. Dai, C. Zhou, J. Yan, L. Wang, Z. Wang, J. Zang, *Bioact. Mater.* **2023**, *26*, 465.
[14] W. Zhao, T. Xu, *Biofabrication* **2020**, *12*, 045020.
[15] M. T. Thai, P. T. Phan, H. A. Tran, C. C. Nguyen, T. T. Hoang, J. Davies, J. Rnjak-Kovacina, H. P. Phan, N. H. Lovell, T. N. Do, *Adv. Sci.* **2023**, *10*, 2205656.
[16] C. Zhou, Y. Yang, J. Wang, Q. Wu, Z. Gu, Y. Zhou, X. Liu, Y. Yang, H. Tang, Q. Ling, *Nat. Commun.* **2021**, *12*, 5072.
[17] J. Burgner-Kahrs, D. C. Rucker, H. Choset, *IEEE Trans. Robot.* **2015**, *31*, 1261.
[18] C. C. Nguyen, S. Wong, M. T. Thai, T. T. Hoang, P. T. Phan, J. Davies, L. Wu, D. Tsai, H. P. Phan, N. H. Lovell, *Adv. Sens. Res.* **2023**, *2*, 2200036.
[19] M. T. Thai, P. T. Phan, T. T. Hoang, S. Wong, N. H. Lovell, T. N. Do, *Adv. Intell. Syst.* **2020**, *2*, 1900138.
[20] R. A. Beasley, *J. Robot.* **2012**, *2012*, 401613.
[21] B. Seeliger, L. L. Swanström, *Curr. Opin. Gastroenterol.* **2020**, *36*, 370.
[22] J. Reisenauer, M. J. Simoff, M. A. Pritchett, D. E. Ost, A. Majid, C. Keyes, R. F. Casal, M. S. Parikh, J. Diaz-Mendoza, S. Fernandez-Bussy, *Ann. Thoracic Surge.* **2022**, *113*, 308.
[23] A. Al Nooryani, W. Aboushokka, *Case Rep. Cardiol.* **2018**, *2018*, 6086034.
[24] Y. Kim, G. A. Parada, S. Liu, X. Zhao, *Sci. Rob.* **2019**, *4*, eaax7329.
[25] J. Rogatinsky, D. Recco, J. Feichtmeier, Y. Kang, N. Kneier, P. Hammer, E. O'Leary, D. Mah, D. Hoganson, N. V. Vasilyev, *Sci. Adv.* **2023**, *9*, eadi5559.
[26] K. Adhikari, S. Tatinati, K. C. Veluvolu, J. A. Chambers, *IEEE Trans. Automat. Sci. Eng.* **2020**, *19*, 497.
[27] D.-H. Lee, Y.-H. Kim, J. Collins, A. Kapoor, D.-S. Kwon, T. Mansi, *IEEE Robot. Automat. Lett.* **2021**, *6*, 1224.
[28] Y. Zhang, X. Wu, R. A. Vadlamani, Y. Lim, J. Kim, K. David, E. Gilbert, Y. Li, R. Wang, S. Jiang, *Adv. Healthcare Mater.* **2023**, *12*, 2300964.
[29] T. Gopesh, J. H. Wen, D. Santiago-Dieppa, B. Yan, J. S. Pannell, A. Khalessi, A. Norbash, J. Friend, *Sci. Rob.* **2021**, *6*, eabf0601.
[30] P. T. Phan, M. T. Thai, T. T. Hoang, J. Davies, C. C. Nguyen, H.-P. Phan, N. H. Lovell, T. N. Do, *Sci. Rep.* **2022**, *12*, 11067.
[31] V. Cacucciolo, J. Shintake, Y. Kuwajima, S. Maeda, D. Floreano, H. Shea, *Nature* **2019**, *572*, 516.
[32] M. Smith, V. Cacucciolo, H. Shea, *Science* **2023**, *379*, 1327.
[33] J. Davies, M. T. Thai, T. T. Hoang, C. C. Nguyen, P. T. Phan, H. P. Phan, N. H. Lovell, T. N. Do, *Adv. Mater. Technol.* **2023**, *8*, 2201453.

[34] S. Xu, Y. Chen, N. P. Hyun, K. P. Becker, R. J. Wood, *Proc. Natl. Acad. Sci. USA* **2021**, *118*, e2103198118.
[35] S. Xu, C. M. Nunez, M. Souri, R. J. Wood, *Sci. Rob.* **2023**, *8*, eadd4649.
[36] S. Yim, S. Miyashita, D. Rus, S. Kim, *IEEE Trans. Robot.* **2017**, *33*, 456.
[37] S. Frishman, R. D. Ings, V. Sheth, B. L. Daniel, M. R. Cutkosky, *IEEE Trans. Med. Robot. Bion.* **2021**, *3*, 701.
[38] T. N. Do, T. E. T. Seah, S. J. Phee, *IEEE Trans. Biomed. Eng.* **2016**, *63*, 1229.
[39] T.-K. Nguyen, S. Yadav, T.-A. Truong, M. Han, M. Barton, M. Leitch, P. Guzman, T. Dinh, A. Ashok, H. Vu, *ACS Nano* **2022**, *16*, 10890.
[40] A. Ashok, T. K. Nguyen, M. Barton, M. Leitch, M. K. Masud, H. Park, T. A. Truong, Y. V. Kaneti, H. T. Ta, X. Li, *Small* **2022**, *19*, 2204946.
[41] Y. Qiu, A. Ashok, C. C. Nguyen, Y. Yamauchi, T. N. Do, H. P. Phan, *Small* **2024**, *20*, 2308805.
[42] T. A. Truong, T. K. Nguyen, X. Huang, A. Ashok, S. Yadav, Y. Park, M. T. Thai, N. K. Nguyen, H. Fallahi, S. Peng, *Adv. Funct. Mater.* **2023**, *33*, 2211781.
[43] C. C. Nguyen, T. T. Hoang, J. Davies, P. T. Phan, M. T. Thai, E. Nicotra, A. A. Abed, H. A. Tran, T. A. Truong, B. Sharma, *Adv. Sci.* **2024**, *11*, 2405610.
[44] F. Karimi, N. Farbehi, F. Ziaee, K. Lau, M. Monfared, M. Kordanovski, H. Joukhdar, T. G. Molly, R. Nordon, K. A. Kilian, *Adv. Funct. Mater.* **2024**, *34*, 2313354.
[45] C. C. Nguyen, M. T. Thai, T. T. Hoang, J. Davies, P. T. Phan, K. Zhu, L. Wu, M. A. Brodie, D. Tsai, Q. P. Ha, *Sens. Actuators, A* **2023**, *357*, 114380.
[46] M. T. Thai, J. Davies, C. C. Nguyen, P. T. Phan, T. T. Hoang, A. Ji, K. Zhu, B. Sharma, E. Nicotra, T. T. Vo-Doan, *Adv. Sens. Res.* **2024**, *3*, 2300105.
[47] P. Zhang, H. Wang, P. Wang, Y. Zheng, L. Liu, J. Hu, Y. Liu, Q. Gao, Y. He, *Bioact. Mater.* **2021**, *6*, 1402.
[48] H. A. Tran, T. T. Hoang, A. Maraldo, T. N. Do, D. L. Kaplan, K. S. Lim, J. Rnjak-Kovacina, *Mater. Today* **2023**, *65*, 244.
[49] C. M. Elvin, T. Vuocolo, A. G. Brownlee, L. Sando, M. G. Huson, N. E. Liyou, P. R. Stockwell, R. E. Lyons, M. Kim, G. A. Edwards, *Biomaterials* **2010**, *31*, 8323.
[50] H. Suzuki, R. J. Wood, *Nat. Mach. Intell.* **2020**, *2*, 437.
[51] S. Yang, R. A. MacLachlan, C. N. Riviere, *IEEE/ASME Trans. Mechatron.* **2014**, *20*, 761.
[52] R. Nuzzi, L. Brusasco, *Eye brain* **2018**, *10*, 13.
[53] R. Dimatteo, N. J. Darling, T. Segura, *Adv. Drug Delivery Rev.* **2018**, *127*, 167.
[54] M. Xu, Z. Song, W. Hong, L. Wang, C. Jiang, B. Yang, M. Qin, J. Liu, *Adv. Funct. Mater.* **2023**, *33*, 2302041.
[55] C. Lv, S. Wang, C. Shi, *Ann. Biomed. Eng.* **2020**, *48*, 669.
[56] C. C. Nguyen, T. Teh, M. T. Thai, P. T. Phan, T. T. Hoang, J. Davies, H.-P. Phan, C. H. Wang, N. H. Lovell, T. N. Do, *IEEE Trans. Med. Robot. Bioni.* **2023**, *5*, 590.
[57] E. A. Allen, J. P. Swensen, presented at *2020 IEEE/RSJ Int. Conf. on Intelligent Robots and Systems (IROS)*, Las Vegas, NV, USA, October, **2020**.
[58] J. Sheng, X. Wang, T.-M. L. Dickfeld, J. P. Desai, *IEEE Robot. Automat. Lett*, IEEE, New York, **2018**, *3*, 4038.